2006 Vol. 39, No. 8 / August 2022 / Journal of the Optical Society of America B

Research Article

Journal of the Optical Society of America B

OPTICAL PHYSICS

Stability of symmetry-protected BICs in dielectric metasurfaces

Bing Meng,[1] Chunjie Feng,[2] Li Chen,[1] Xiaoying Qu,[1] Xinfeng Wang,[1] and Chaobiao Zhou[1,*]

[1]College of Mechanical and Electronic Engineering, Guizhou Minzu University, Guiyang 550025, China
[2]School of Mathematics and Physics, Anshun University, Anshun 561000, China
*Corresponding author: cbzhou@gzmu.edu.cn

Received 6 June 2022; revised 19 June 2022; accepted 19 June 2022; posted 21 June 2022; published 5 July 2022

Optical metasurfaces with high *Q*-factors have attracted much attention due to their sharp spectral features and significant field enhancement. The excitation of symmetry-protected bound states in the continuum (SP-BICs) is an efficient way to achieve a high *Q*-factor resonator. The experimental *Q*-factors of resonant quasi-SP-BIC metasurfaces are currently not high. In this work, we numerically demonstrate the stability of SP-BICs in silicon metasurfaces. The two SP-BICs are transformed into quasi-SP-BICs by breaking the in-plane symmetry of the structure, and their resonance properties are discussed by far-field radiation and near-field distribution. Moreover, the effects of different periods, sizes, substrate refractive indices, and shape factors on the SP-BICs are explored, and the *Q*-factors of quasi-SP-BICs always exhibit the same inverse quadratic dependence on asymmetry parameters, which demonstrates the stability of the SP-BIC. Our results may provide theoretical support for the experimental realization of ultrahigh *Q*-factor quasi-SP-BICs.

https://doi.org/10.1364/JOSAB.465997

1. INTRODUCTION

In recent years, the study of high *Q*-factor metasurfaces has attracted much attention due to their ability to significantly enhance the interaction between light and matter [1–6]. Bound states in the continuum (BICs) belong to ideal optical local modes embedded in the continuous background spectrum [7–10]. In fact, BICs are a special class of resonant leakage modes that have infinite *Q*-factors or zero radiation loss. Normally, BICs must be converted into quasi-BICs with ultrahigh *Q*-factors to be excited by external light sources [11–25]. Accompanied by the excitation of quasi-BICs, the electromagnetic field has an extremely strong local effect. Therefore, quasi-BICs are widely used to enhance light–matter interactions. Symmetry-protected BICs (SP-BICs), Friedrich–Wintgen BICs, and Fabry–Perot BICs are three common BICs [7]. Among them, SP-BICs are the easiest to realize experimentally, and can be transformed into quasi-SP-BICs by breaking the symmetry of their structures. In 2018, Koshelev *et al.* analyzed and summarized the high *Q*-factor properties of various metal or dielectric metasurfaces with symmetry breaking [12]. They found that the strong Fano resonance originates from the perturbation of SP-BICs, and proposed that the *Q*-factor can be easily adjusted by the asymmetry parameter α. The *Q*-factor satisfies the following equation: $Q \propto \alpha^{-2}$. It is clear that the smaller α is, the larger the *Q*-factor is. Currently, there are two main ways to excite SP-BICs. One is to introduce the size discord by breaking the geometric symmetry of the structure, such as split rings [26,27], asymmetric nanorods [28–30], notched cubes [31,32], and notched disks [14,33,34]. Another is to introduce position discord by changing the relative positions of composite elements of metasurfaces [35,36].

Quasi-BIC metasurfaces with high *Q*-factors have three important properties, namely, a sharp resonance spectrum, significant local field enhancement, and large-area interactions between light and matter. Therefore, they are widely used in various nanophotonic devices with high performance, such as ultralow-threshold lasers [37–39], chemical and biological sensors [40,41], electro-optic modulators [42], nonlinear optical devices [43–47], and so on. However, compared to systems such as whispering gallery microcavities or photonic crystal defect cavities, this resonant quasi-BIC metasurface has relatively lower experimental *Q*-factors. The main reasons for this are twofold: on one hand, the imperfection of the device is introduced in the fabrication process; on the other hand, the coupling efficiency is low due to the limitation of the detection equipment [48]. In recent years, to improve the experimental *Q*-factor, researchers have proposed various schemes. In theory, the protection characteristics of topology are used to improve the fabrication tolerance of quasi-BICs, and the cross polarization method is used to improve detection efficiency [1,2]. Recently, Abujetas *et al.* verified this the robust response of BICs at terahertz frequencies in gold-rod dimers by measuring the reduction in linewidth and in increase in the lifetimes of

quasi-BICs [49]. A more direct and complete demonstration about the stability of SP-BICs is lacking.

In this work, by numerical simulation methods, we demonstrate the stability of SP-BICs in dielectric metasurfaces. First, two non-radiative SP-BICs are transformed into quasi-SP-BICs by changing the size of the composite elements. Then, the effects of the parameters of the period, radius, substrate refractive index, and shape factors on SP-BICs are investigated, which verify that the Q-factor and asymmetry parameter α always satisfy the fundamental criterion of SP-BICs: $Q \propto \alpha^{-2}$. Thus, the stability of SP-BICs and its large fabrication tolerance are numerically confirmed, which provides theoretical support for the experimental realization of quasi-SP-BICs with ultrahigh Q-factors.

2. SYMMETRY-PROTECTED BICs IN SILICON METASURFACE

An oligomer metasurface consisting of four semicircular Si nanodisks is designed. The period of the unit cell is $P_x = P_y = 1000$ nm, where each disk has a radius R_0 of 200 nm and height of 220 nm, and the nanodisks are labeled D1, D2, D3, and D4. A SiO_2 substrate is placed under the nanodisk array. We change the size of one nanodisk to break the symmetry of structure along the y axis, and the SP-BIC is transformed into a quasi-SP-BIC with a Fano profile. As shown in Fig. 1(a), taking changing the radius of D4 as an example, the increased radius is denoted as R, and then the radius change is $\Delta R = R - R_0$. Herein, the finite difference time domain method (FDTD Solutions) is employed to analyze the optical properties of metasurfaces. The incident light propagates along the z axis and the electric field along the y axis. The periodic boundary conditions in x and y directions are used, and the perfect matching layer in the z direction is applied. The dielectric constants of Si and SiO_2 are extracted from Ref. [50]. Figure 1(b) shows the transmission spectrum mapping when the radius of nanodisk D4 is gradually increased. When R is larger than zero, the two SP-BICs are excited as leaky mode quasi-SP-BICs (QBICs), and the resonance spectra are gradually broadened as R increases. The wavelengths of the two BICs labeled as BIC-1 and BIC-2 are about 1470 and 1550 nm, respectively. For an intuitive comparison, the transmission spectra at $R = 0$ and $R = 30$ nm are exhibited in Fig. 1(c). The two sharp resonances are observed near wavelengths 1485 and 1575 nm, labeled as QBIC-1 and QBIC-2, respectively. The results reveal that the symmetry metasurfaces ($\Delta R = 0$ nm) support two SP-BIC modes, and two asymmetry Fano resonances are generated when introducing the symmetry breaking of nanodisk oligomers. It is worth noting that the spectrum of QBIC-2 is narrower than QBIC-1 for the same ΔR. As shown in Fig. 1(d), we calculated the Q-factors corresponding to QBIC-1 and QBIC-2 for different ΔR, and made a data fit with $y = Ax^{-2}$. The Q-factors of both QBICs satisfy the relation $Q \propto \Delta R^{-2}$, and the fitting coefficient of QBIC-2 is larger than QBIC-1, so for the same ΔR, the Q-factor of QBIC-2 is larger. Herein, the asymmetry degree is defined as $\alpha = \Delta R / R_0$, and R_0 is the radius of the original nanodisk; thus, $Q \propto \alpha^{-2}$. As a result, it is confirmed that the two BICs belong to SP-BICs.

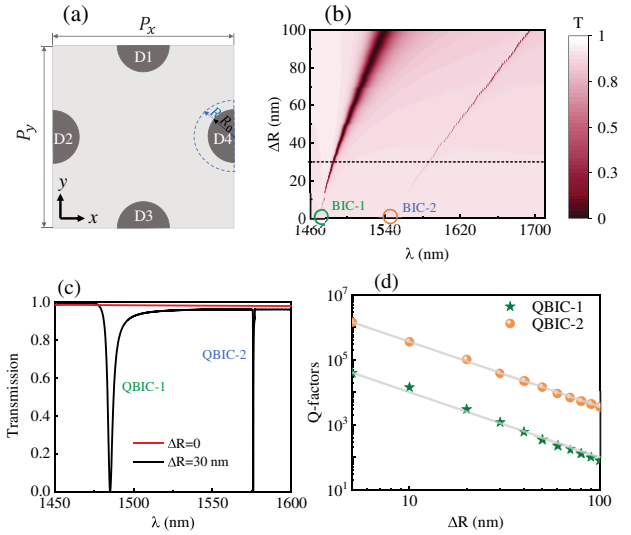

Fig. 1. (a) Top view of unit cell of the semicircular nanodisk metasurface. R_0 is the initial radius of the disk, and R is the radius after the change of disk D4. (b) Transmission mapping versus wavelength λ and parameter ΔR. (c) Transmission spectra for $\Delta R = 0$ and $\Delta R = 30$ nm. (d) Log–log plot of Q-factors as a function of the asymmetry parameter ΔR for QBIC-1 and QBIC-2.

The Fano profiles of QBICs arise from the coupling between the discrete bound states supported by dielectric nanodisks and the free space continuum, and their resonance curves can be described by the Fano formula [51–53]

$$T(\omega) = T_0 + A_0 \frac{[q + 2(\omega - \omega_0)/\tau]^2}{1 + [2(\omega - \omega_0)/\tau]^2}, \tag{1}$$

where ω_0 is the resonant frequency, τ is the resonance linewidth, T_0 is the background scattering parameter, A_0 is the coupling coefficient between the continuous and discrete states, and q is the Breit–Wigner–Fano parameter, which determines the asymmetry of the resonance spectrum. The Q-factor is evaluated by $\frac{\omega_0}{\tau}$. The fitted results for two QBICs are shown in Figs. 2(a) and 2(b), and the Q-factors of QBIC-1 and QBIC-2 are 1092 and 7531, respectively.

To further analyze the resonance properties of the two QBICs, the multipole decomposition of the resonance modes in Cartesian coordinates is performed [54–56]. The calculation results of QBIC-1 are shown in Fig. 2(b). The far-field radiation from the magnetic dipole is the main contribution at resonance wavelength, and the toroidal dipole and electric quadrupole account for the obvious contribution. It is worth pointing out that the radiation power of these dipoles is comparable. Therefore, for QBIC-1, the interference between multiple dipoles will be more obvious. In Fig. 2(c), the displacement current distribution is simulated for further confirmation. It is clear that the displacement current vector does not have a specific distribution, and is formed by the coupling of the magnetic dipole, toroidal dipole, and electric quadrupole to each other. For QBIC-2, as shown in Fig. 2(e), the multipole decomposition exhibits that the far-field radiation contribution of the electric quadrupole dominates at the resonance wavelength, and the other dipoles are strongly suppressed. The corresponding displacement current distribution is indeed

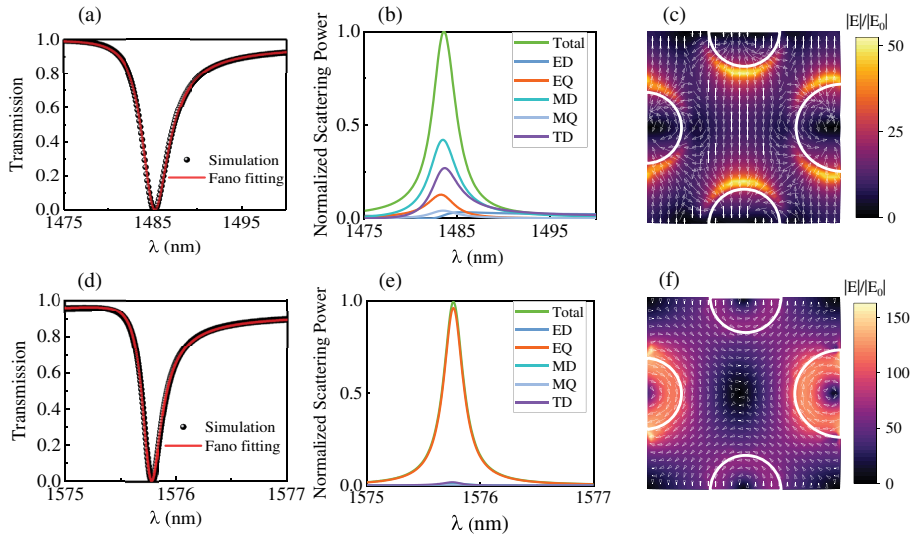

Fig. 2. (a), (d) Fano fitting of QBIC-1 and QBIC-2 for $\Delta R = 30$ nm. (b), (e) Normalized scattered power of different multipoles. (c), (f) Electric field and the displacement current distributions of QBIC-1 and QBIC-2.

an electric quadrupole distribution, as shown in Fig. 2(f). In addition, the local field enhancement of QBIC-1 occurs mainly at the edge of the four nanodiks, while the near-field enhancement of QBIC-2 is mainly in the interior of D2 and D4, and its maximum field enhancement is larger than that of QBIC-1. The strong resonance of QBICs in metasurfaces is ascribed to the array effect [13,31,57,58]. As the number of elements increases, the edge loss in the transverse plane gradually decreases; the Q-factor gradually increases, and it will reach saturation at a certain number of elements. The near-field distribution and far-field scattering intensity are mutually corroborated. These results reveal that the two modes are distinctly different. It is noted that the resonance spectra can be significantly modulated when the incident angle θ is changed (details in Appendix A).

3. STABILITY OF SYMMETRY-PROTECTED BICs

We have demonstrated that the two BICs are governed by SP-BICs. Next, we study the stability of SP-BICs by exploring the effects of the period, nanodisk radius, substrate refractive index, and shape on the relation $Q \propto \Delta R^{-2}$.

First, the influence of the period of a matesurface on the two modes is analyzed. We fix the periods as $P = 900$ nm and $P = 1100$ nm to compare with the previous results. The same symmetry breaking in y direction is introduced by changing the size of nanodisk D4, and the two same modes are excited after introducing symmetry breaking. The Q-factors of the two QBICs still satisfy $Q \propto \Delta R^{-2}$ as shown in Fig. 3(a). Therefore, BIC-1 and BIC-2 still exist at different periods. When the period is changed from 900 to 1100 nm, the Q-factor undergoes a small increase due to the change in the coupling effect between nanodisks. It is worth pointing out that for large perturbation parameters, the complex interactions will change, inducing a large detuning of the Q-factor with ΔR^{-2} [59]. As illustrated in Fig. 3(b), the resonance wavelengths of QBIC-1 and QBIC-2 show different degrees of redshift as the period increases. The period has less effect on the resonance wavelength of QBIC-2,

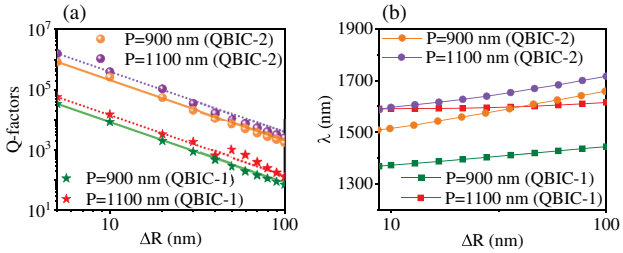

Fig. 3. Variation of (a) Q-factor and (b) resonance wavelength with ΔR for different periods.

while it has more obvious influence on that of QBIC-1. In addition, ΔR shows a smaller effect on the resonance wavelength of QBIC-1, and a more significant influence on QBIC-2. Therefore, as the period and ΔR increase, the resonance wavelengths of the two QBICs may overlap. For example, when ΔR is about 55 nm, the resonance wavelength of QBIC-1 at $P = 1100$ nm intersects that of QBIC-2 at $P = 900$ nm.

In the following, we analyze the effect of the radius of the nanodisk on the two BICs, fixing the radii as $R = 180$ nm and $R = 220$ nm, respectively. The simulation conditions are the same as the previous settings, and the two modes are excited when the size of D4 is changed. As shown in Fig. 4(a), it is clear that the change of Q-factor is small when the radius R is increased, and $Q \propto \Delta R^{-2}$, so the two BICs are stable. As exhibited in Fig. 4(b), the change of radius leads to a different degree of redshift in the resonance wavelengths of the two QBICs, which is mainly due to the increase in effective refractive index of the silicon metasurfaces with the increase in radius. It is worth noting that when $R = 220$ nm, the resonance wavelengths of QBIC-1 and QBIC-2 overlap at ΔR of about 65 nm. At this time, the two QBICs are significantly coupled.

Next, we discuss the effect of substrate refractive index on the two BICs. The substrate refractive indices are fixed to $n = 1.3$ and $n = 1.6$, respectively, and we change the size of nanodisk D4 in the same way, as shown in Fig. 5(a). The Q-factor and

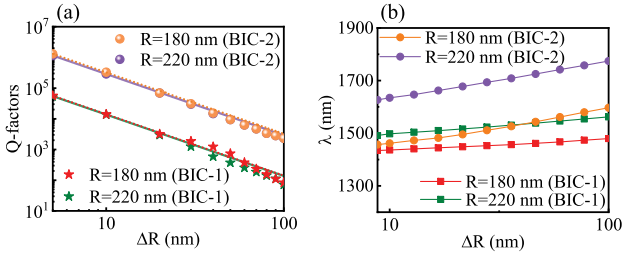

Fig. 4. Variation of (a) Q-factor and (b) resonance wavelength with ΔR at different nanodisk radii.

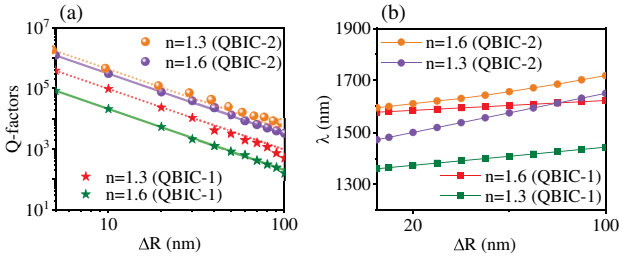

Fig. 5. Variation of (a) Q-factor and (b) resonance wavelength with asymmetry ΔR for different substrate refractive indices.

ΔR still show a relationship of -2nd power, so the BICs are stable when the substrate refractive index is properly changed. As n increases, the Q-factors of the two QBICs decrease due to the leakage of the optical field to the substrate. The Q-factor of QBIC-1 is more significantly affected by the n value, while the effect of n on QBIC-2 is less. From Fig. 5(b), it is clear that the increase in n also leads to a different degree of redshift in the resonance wavelengths of QBIC-1 and QBIC-2. The resonance wavelengths of QBIC-1 ($n = 1.6$) and BIC-2 ($n = 1.3$) overlap when ΔR is about 80 nm.

Finally, we discuss the effect of device shape on BICs. The nanostructure is changed into a rectangular nanodisk or isosceles trapezoidal nanodisk metasurface with the same volume. The top view of the rectangular nanodisk is shown in Fig. 6(a), where the period P of the unit cell is still 1000 nm, the initial length L_0 of each nanodisk is 355 nm, the width is $L_0/2$, and the height is 220 nm. We also mark the four nanosiks as D1, D2, D3, and D4, and label the enlarged length of nanodisk D4 as L. The changed length is denoted as ΔL, where $\Delta L = L - L_0$, and the asymmetry degree is defined as $\alpha_1 = \Delta L/L_0$. The symmetry of the structure along y axis is broken when the size of D4 is enlarged, and the same resonance modes are excited. Figure 6(d) shows the top view of the isosceles trapezoidal nanodisks, where the period P is still 1000 nm, the upper bottom and waist length of each disk is noted as W_0, and the size is 219 nm. The lower bottom length is $2W_0$, and the height is 220 nm. We mark the nanodisk in the same way; the enlarged side length of D4 is noted as W, its change $\Delta W = W - W_0$, and the asymmetry degree is defined as $\alpha_2 = \Delta W/W_0$. As illustrated in Figs. 6(b) and 6(e), the Q-factors exhibit the same inverse quadratic dependence on asymmetry parameters (ΔL, ΔW), so the two modes are still governed by SP-BICs. The results reveal that SP-BICs are robust when the shape of the device is slightly changed. As shown in Figs. 6(c) and 6(f), the resonance wavelengths are redshifted as the asymmetry parameter increases. In addition, the transmission spectra, multipole decomposition, and near-field distribution of QBIC-2 for rectangular and isosceles trapezoidal nanodisk metasurfaces are caculated in Fig. 9. These resonance properties are consistent with those of the previous semicircular nanodisks. If these device shapes are changed to triangular nanodisks or other structures, the BICs still exist. Therefore, SP-BICs exhibit strong stability for device shape.

It is noted that the difference between R (L, W) and R_0 (L_0, W_0) perturbs the in-plane symmetry of the structure, degenerating the higher order group C_{4v} to lower order group C_s, and leads to the access of leaky quasi-BIC states from true BIC states. Therefore, the QBIC excitation depends on the polarization of the incident plane wave. In addition, The samples can be fabricated on a Si on glass wafer. The fabrication processes mainly

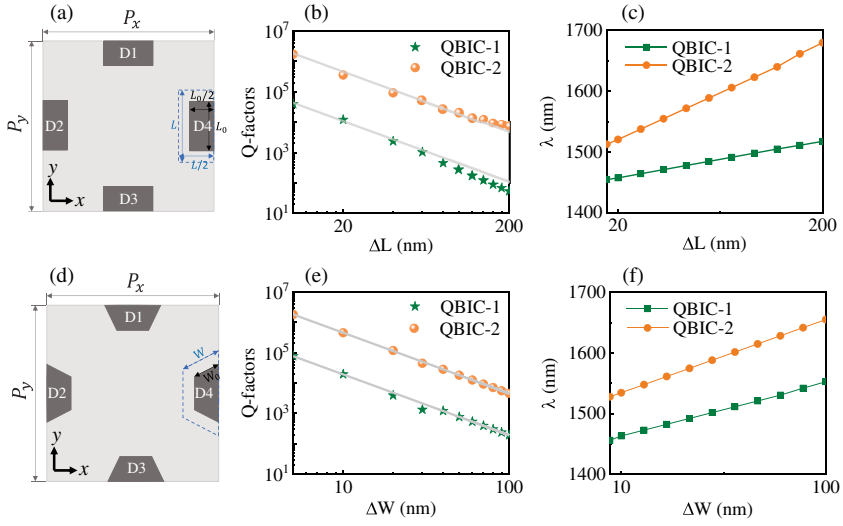

Fig. 6. Top view of unit cell of the (a) rectangular and (d) isosceles trapezoidal nanodisk metasurfaces. (b), (e), (c) and (f) Variation of Q-factors and resonance wavelength with asymmetry parameters for both nanostructures.

include electron-beam lithography (EBL) and inductively coupled plasma (ICP) etching techniques.

4. CONCLUSION

In summary, we investigated the stability of SP-BIC in dielectric metasurfaces. The two individual BICs can be transformed into QBICs by breaking the in-plane symmetry of the structure. The resonance properties of these QBICs are discussed by performing far-field contributions and near-field analysis. Moreover, the effects of different periods, sizes, substrate refractive indices, and shape factors on BICs are studied, and the same inverse quadratic dependence of Q-factors for QBICs excited by changing the size of nanodisk D4 on the asymmetry parameters (ΔR, ΔL, ΔW) is observed and explained in detail. These results confirm the very strong stability of SP-BICs. In practice, the deviations from the theoretical design are impossible to avoid, and the robust SP-BICs may facilitate the realization of high Q-factors in experiment.

APPENDIX A: EFFECT OF INCIDENT ANGLE θ OF LIGHT ON QBICs

In Fig. 7, we calculate the transmission spectra and Q-factors of different incident light angles θ for $\Delta R = 100$ nm. The resonance spectrum is sensitive to the incident angle of light. When θ is increased, there is only part of light coupling to the device to participate in the interaction between light and material, and the extinction ratio of the resonance spectra become low gradually. The resonance linewidth is not affected by θ, and their Q-factors remain constant. In a real situation, the coupling efficiency of light and a metasurface is affected by the incident light angles. If ultrahigh Q-factors are observed in experiment, a vertical incident light needs to be ensured.

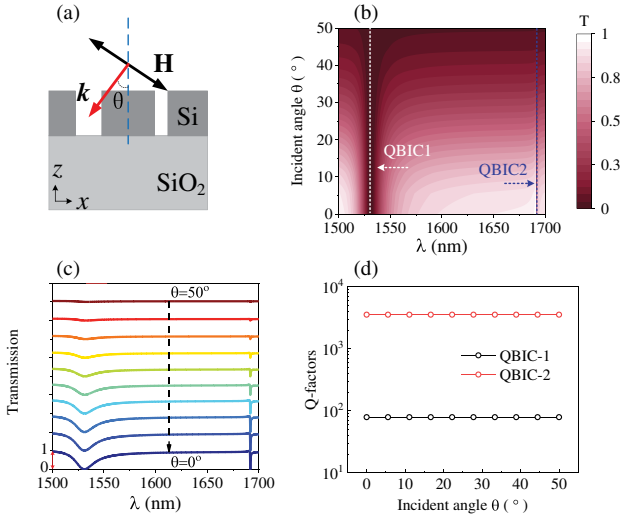

Fig. 7. Dependence of resonance on the incident angle θ of light for circular nanodisk metasurface. (a) Sketches of θ. (b) Transmission mapping versus different θ and wavelengths. (c), (d) Corresponding transmission spectra and Q-factors.

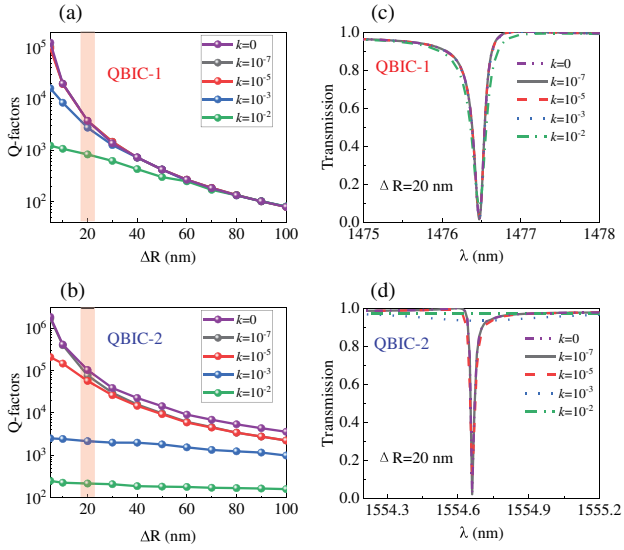

Fig. 8. (a), (b) Q-factors of QBIC-1 and QBIC-2 as a function of asymmetry parameter ΔR under different extinction coefficients for losses in silicon, respectively. (c), (d) Transmission spectra for different loss levels; $\Delta R = 20$ nm.

APPENDIX B: EFFECT OF DIFFERENT EXTINCTION COEFFICIENTS (k) IN SILICON ON QBICs

In Figs. 8(a) and 8(b), the effects of different extinction coefficients (k) in silicon on Q-factors of QBIC-1 and QBIC-2 are calculated. The Q-factor decreases dramatically with the increase in k for small ΔR. When the value of ΔR is increased, the Q-factor is low and the effect of k is small. In Figs. 8(c) and 8(d), the transmission spectra for different loss levels are shown under $\Delta R = 20$ nm. For QBIC-2 with a high Q-factor, with the increase in k, the transmission spectrum widens rapidly and the extinction ratio decreases. For low Q-factor QBIC-1, k has little effect on the resonance spectra [60,61].

APPENDIX C: RESONANCE PROPERTIES OF QBIC-2 FOR RECTANGULAR NANODISK AND ISOSCELES TRAPEZOIDAL NANODISK METASURFACES

Since the symmetry of the device is unchanged, the resonance properties of QBIC excited by rectangular nanodisk or isosceles trapezoidal nanodisk metasurfaces are consistent with those of the circular nanodisk metesurface. Here, we calculate the transmission spectrum, multipole decomposition, and near-field distribution of QBIC-2, and the results reveal that the leakage mode QBIC-2 is still an electric quadrupole resonance.

Funding. National Natural Science Foundation of China (12004084, 12164008); Guizhou Provincial Science and Technology Projects (ZK[2021]030, ZK[2022]203); Youth Science and Technology Talent Project of Guizhou Province (KY[2021]105); Natural Science Research Project of Guizhou Minzu University (GZMUZK[2021]YB06, GZMUZK[2021]YB08); Undergraduate Innovation and Entrepreneurship Training Program of Guizhou Province (202110672110).

Disclosures. The authors declare no conflicts of interest.

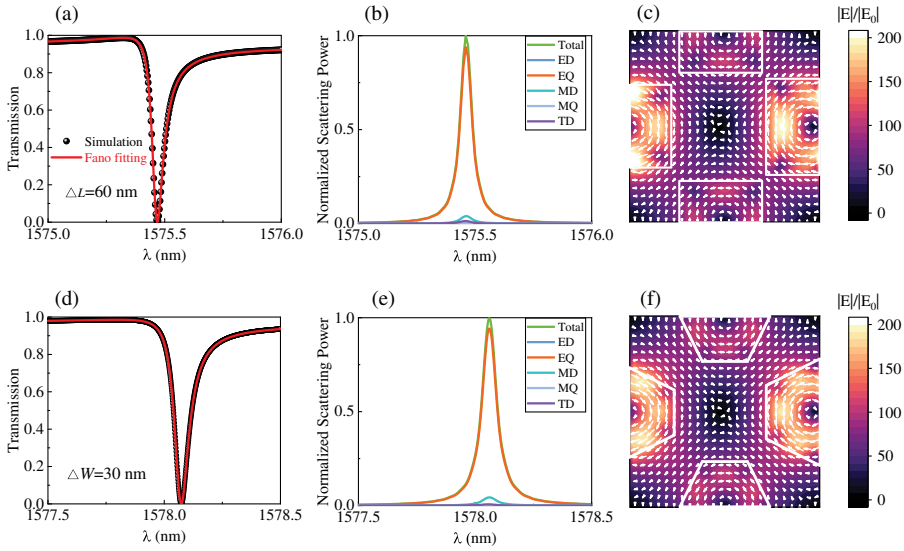

Fig. 9. (a), (d) Fano fitting of QBIC-1 and QBIC-2 for $\Delta L = 30$ nm, $\Delta W = 60$ nm. (b), (e) Normalized scattered power of different multipoles. (c), (f) Electric field and the displacement current distributions of QBIC-1 and QBIC-2.

Data availability. Data underlying the results presented in this paper are not publicly available at this time but may be obtained from the authors upon reasonable request.

REFERENCES

1. J. Jin, X. Yin, L. Ni, M. Soljačić, B. Zhen, and C. Peng, "Topologically enabled ultrahigh-Q guided resonances robust to out-of-plane scattering," Nature **574**, 501–504 (2019).
2. Z. Chen, X. Yin, J. Jin, Z. Zheng, Z. Zhang, F. Wang, L. He, B. Zhen, and C. Peng, "Observation of miniaturized bound states in the continuum with ultra-high quality factors," Sci. Bull. **67**, 359–366 (2022).
3. M. S. Bin-Alam, O. Reshef, Y. Mamchur, M. Z. Alam, G. Carlow, J. Upham, B. T. Sullivan, J.-M. Ménard, M. J. Huttunen, R. W. Boyd, and K. Dolgaleva, "Ultra-high-Q resonances in plasmonic metasurfaces," Nat. Commun. **12**, 974 (2021).
4. M. F. Limonov, M. V. Rybin, A. N. Poddubny, and Y. S. Kivshar, "Fano resonances in photonics," Nat. Photonics **11**, 543–554 (2017).
5. H. Zhu, Z. Xu, L. Cai, H. Wang, H. Luo, A. Pattanayak, P. Ghosh, M. Qiu, and Q. Li, "Ultrathin high quality-factor planar absorbers/emitters based on uniaxial/biaxial anisotropic van der Waals polar crystals," Adv. Opt. Mater. **9**, 2100645 (2021).
6. V. Ardizzone, F. Riminucci, S. Zanotti, A. Gianfrate, M. Efthymiou-Tsironi, D. Suàrez-Forero, F. Todisco, M. De Giorgi, D. Trypogeorgos, G. Gigli, K. Baldwin, L. Pfeiffer, D. Ballarini, H. S. Nguyen, D. Gerace, and D. Sanvitto, "Polariton Bose–Einstein condensate from a bound state in the continuum," Nature **605**, 447–452 (2022).
7. C. W. Hsu, B. Zhen, A. D. Stone, J. D. Joannopoulos, and M. Soljačić, "Bound states in the continuum," Nat. Rev. Mater. **1**, 1–13 (2016).
8. Y. Jahani, E. R. Arvelo, F. Yesilkoy, K. Koshelev, C. Cianciaruso, M. De Palma, Y. Kivshar, and H. Altug, "Imaging-based spectrometer-less optofluidic biosensors based on dielectric metasurfaces for detecting extracellular vesicles," Nat. Commun. **12**, 3246 (2021).
9. L. Huang, L. Xu, M. Woolley, and A. E. Miroshnichenko, "Trends in quantum nanophotonics," Adv. Quantum Technol. **3**, 1900126 (2020).
10. S. Joseph, S. Pandey, S. Sarkar, and J. Joseph, "Bound states in the continuum in resonant nanostructures: an overview of engineered materials for tailored applications," Nanophotonics **10**, 4175–4207 (2021).
11. A. S. Kupriianov, Y. Xu, A. Sayanskiy, V. Dmitriev, Y. S. Kivshar, and V. R. Tuz, "Metasurface engineering through bound states in the continuum," Phys. Rev. Appl. **12**, 014024 (2019).
12. K. Koshelev, S. Lepeshov, M. Liu, A. Bogdanov, and Y. Kivshar, "Asymmetric metasurfaces with high-Q resonances governed by bound states in the continuum," Phys. Rev. Lett. **121**, 193903 (2018).
13. S. Li, C. Zhou, T. Liu, and S. Xiao, "Symmetry-protected bound states in the continuum supported by all-dielectric metasurfaces," Phys. Rev. A **100**, 063803 (2019).
14. C. Zhou, X. Qu, S. Xiao, and M. Fan, "Imaging through a Fano-resonant dielectric metasurface governed by quasi–bound states in the continuum," Phys. Rev. Appl. **14**, 044009 (2020).
15. J. Yu, B. Ma, A. Ouyang, P. Ghosh, H. Luo, A. Pattanayak, S. Kaur, M. Qiu, P. Belov, and Q. Li, "Dielectric super-absorbing metasurfaces via PT symmetry breaking," Optica **8**, 1290–1295 (2021).
16. R. M. Saadabad, L. Huang, and A. E. Miroshnichenko, "Polarization-independent perfect absorber enabled by quasibound states in the continuum," Phys. Rev. B **104**, 235405 (2021).
17. C. Zhou, T. Pu, J. Huang, M. Fan, and L. Huang, "Manipulating optical scattering of quasi-BIC in dielectric metasurface with off-center hole," Nanomaterials **12**, 54 (2021).
18. P. Xie, Z. Liang, T. Jia, D. Li, Y. Chen, P. Chang, H. Zhang, and W. Wang, "Strong coupling between excitons in a two-dimensional atomic crystal and quasibound states in the continuum in a two-dimensional all-dielectric asymmetric metasurface," Phys. Rev. B **104**, 125446 (2021).
19. W. Huang, S. Liu, Y. Cheng, J. Han, S. Yin, and W. Zhang, "Universal coupled theory for metamaterial bound states in the continuum," New J. Phys. **23**, 093017 (2021).
20. J. Algorri, F. Dell'Olio, P. Roldán-Varona, L. Rodrguez-Cobo, J. López-Higuera, J. Sánchez-Pena, and D. Zografopoulos, "Strongly resonant silicon slot metasurfaces with symmetry-protected bound states in the continuum," Opt. Express **29**, 10374–10385 (2021).
21. M. Qin, S. Xiao, W. Liu, M. Ouyang, T. Yu, T. Wang, and Q. Liao, "Strong coupling between excitons and magnetic dipole quasi-bound states in the continuum in WS_2-TiO_2 hybrid metasurfaces," Opt. Express **29**, 18026–18036 (2021).
22. M. Qin, J. Duan, S. Xiao, W. Liu, T. Yu, T. Wang, and Q. Liao, "Manipulating strong coupling between exciton and quasi-bound states in the continuum resonance via generalized temporal coupled mode theory," Phys. Rev. B **105**, 195425 (2022).
23. H. Li, S. Yu, L. Yang, and T. Zhao, "High Q-factor multi-Fano resonances in all-dielectric double square hollow metamaterials," Opt. Laser Technol. **140**, 107072 (2021).
24. I. A. Al-Ani, K. As' Ham, L. Huang, A. E. Miroshnichenko, and H. T. Hattori, "Enhanced strong coupling of TMDC monolayers by bound state in the continuum," Laser Photon. Rev. **15**, 2100240 (2021).

25. A. C. Overvig, S. C. Malek, M. J. Carter, S. Shrestha, and N. Yu, "Selection rules for quasibound states in the continuum," Phys. Rev. B **102**, 035434 (2020).
26. L. Cong and R. Singh, "Symmetry-protected dual bound states in the continuum in metamaterials," Adv. Opt. Mater. **7**, 1900383 (2019).
27. V. Fedotov, M. Rose, S. Prosvirnin, N. Papasimakis, and N. Zheludev, "Sharp trapped-mode resonances in planar metamaterials with a broken structural symmetry," Phys. Rev. Lett. **99**, 147401 (2007).
28. J. Zhang, K. F. MacDonald, and N. I. Zheludev, "Near-infrared trapped mode magnetic resonance in an all-dielectric metamaterial," Opt. Express **21**, 26721–26728 (2013).
29. K. Koshelev, Y. Tang, K. Li, D.-Y. Choi, G. Li, and Y. Kivshar, "Nonlinear metasurfaces governed by bound states in the continuum," ACS Photon. **6**, 1639–1644 (2019).
30. S. Xiao, X. Wang, J. Duan, T. Liu, and T. Yu, "Engineering light absorption at critical coupling via bound states in the continuum," J. Opt. Soc. Am. B **38**, 1325–1330 (2021).
31. S. Campione, S. Liu, L. I. Basilio, L. K. Warne, W. L. Langston, T. S. Luk, J. R. Wendt, J. L. Reno, G. A. Keeler, I. Brener, and M. B. Sinclair, "Broken symmetry dielectric resonators for high quality factor Fano metasurfaces," ACS Photon. **3**, 2362–2367 (2016).
32. Z. Liu, Y. Xu, Y. Lin, J. Xiang, T. Feng, Q. Cao, J. Li, S. Lan, and J. Liu, "High-*Q* quasibound states in the continuum for nonlinear metasurfaces," Phys. Rev. Lett. **123**, 253901 (2019).
33. J. Wang, J. Kühne, T. Karamanos, C. Rockstuhl, S. A. Maier, and A. Tittl, "All-dielectric crescent metasurface sensor driven by bound states in the continuum," Adv. Funct. Mater. **31**, 2104652 (2021).
34. Z. Zheng, A. Komar, K. Zangeneh Kamali, J. Noble, L. Whichello, A. E. Miroshnichenko, M. Rahmani, D. N. Neshev, and L. Xu, "Planar narrow bandpass filter based on Si resonant metasurface," J. Appl. Phys. **130**, 053105 (2021).
35. Y. Wang, Z. Han, Y. Du, and J. Qin, "Ultrasensitive terahertz sensing with high-*Q* toroidal dipole resonance governed by bound states in the continuum in all-dielectric metasurface," Nanophotonics **10**, 1295–1307 (2021).
36. B. Meng, J. Wang, C. Zhou, and L. Huang, "Bound states in the continuum supported by silicon oligomer metasurfaces," Opt. Lett. **47**, 1549–1552 (2022).
37. M.-S. Hwang, H.-C. Lee, K.-H. Kim, K.-Y. Jeong, S.-H. Kwon, K. Koshelev, Y. Kivshar, and H.-G. Park, "Ultralow-threshold laser using super-bound states in the continuum," Nat. Commun. **12**, 4135 (2021).
38. J.-H. Yang, Z.-T. Huang, D. N. Maksimov, P. S. Pankin, I. V. Timofeev, K.-B. Hong, H. Li, J.-W. Chen, C.-Y. Hsu, Y.-Y. Liu, T.-C. Lu, T.-R. Lin, C.-S. Yang, and K.-P. Chen, "Low-threshold bound state in the continuum lasers in hybrid lattice resonance metasurfaces," Laser Photon. Rev. **15**, 2100118 (2021).
39. A. Kodigala, T. Lepetit, Q. Gu, B. Bahari, Y. Fainman, and B. Kanté, "Lasing action from photonic bound states in continuum," Nature **541**, 196–199 (2017).
40. F. Yesilkoy, E. R. Arvelo, Y. Jahani, M. Liu, A. Tittl, V. Cevher, Y. Kivshar, and H. Altug, "Ultrasensitive hyperspectral imaging and biodetection enabled by dielectric metasurfaces," Nat. Photonics **13**, 390–396 (2019).
41. H. Altug, S.-H. Oh, S. A. Maier, and J. Homola, "Advances and applications of nanophotonic biosensors," Nat. Nanotechnol. **17**, 5–16 (2022).
42. I.-C. Benea-Chelmus, S. Mason, M. L. Meretska, D. L. Elder, D. Kazakov, A. Shams-Ansari, L. R. Dalton, and F. Capasso, "Gigahertz free-space electro-optic modulators based on Mie resonances," Nat. Commun. **13**, 3170 (2022).
43. G. Zograf, K. Koshelev, A. Zalogina, V. Korolev, R. Hollinger, D.-Y. Choi, M. Zuerch, C. Spielmann, B. Luther-Davies, D. Kartashov, S. V. Makarov, S. S. Kruk, and Y. Kivshar, "High-harmonic generation from resonant dielectric metasurfaces empowered by bound states in the continuum," ACS Photon. **9**, 567–574 (2022).
44. L. Xu, K. Zangeneh Kamali, L. Huang, M. Rahmani, A. Smirnov, R. Camacho-Morales, Y. Ma, G. Zhang, M. Woolley, D. Neshev, and A. E. Miroshnichenko, "Dynamic nonlinear image tuning through magnetic dipole quasi-BIC ultrathin resonators," Adv. Sci. **6**, 1802119 (2019).
45. L. Xu, D. A. Smirnova, R. Camacho-Morales, R. A. Aoni, K. Z. Kamali, M. Cai, C. Ying, Z. Zheng, A. E. Miroshnichenko, D. N. Neshev, and M. Rahmani, "Enhanced four-wave mixing from multi-resonant silicon dimer-hole membrane metasurfaces," New J. Phys. **24**, 035002 (2022).
46. C. Zhou, S. Li, C. Gong, Y. Wang, X. Liu, and M. Zhan, "Resonant asymmetric all-dielectric metasurface for boosting third-harmonic generation," arXiv:2004.01088 (2020).
47. A. P. Anthur, H. Zhang, R. Paniagua-Dominguez, D. A. Kalashnikov, S. T. Ha, T. W. Maß, A. I. Kuznetsov, and L. Krivitsky, "Continuous wave second harmonic generation enabled by quasi-bound-states in the continuum on gallium phosphide metasurfaces," Nano Lett. **20**, 8745–8751 (2020).
48. J. Kühne, J. Wang, T. Weber, L. Kühner, S. A. Maier, and A. Tittl, "Fabrication robustness in BIC metasurfaces," Nanophotonics **10**, 4305–4312 (2021).
49. D. R. Abujetas, N. Van Hoof, S. ter Huurne, J. G. Rivas, and J. A. Sánchez-Gil, "Spectral and temporal evidence of robust photonic bound states in the continuum on terahertz metasurfaces," Optica **6**, 996–1001 (2019).
50. E. D. Palik, ed. *Handbook of Optical Constants of Solids*, Vol. **3** (Academic Press, 1998).
51. C. Zhou, S. Li, Y. Wang, and M. Zhan, "Multiple toroidal dipole Fano resonances of asymmetric dielectric nanohole arrays," Phys. Rev. B **100**, 195306 (2019).
52. I. S. Maksymov and A. E. Miroshnichenko, "Active control over nanofocusing with nanorod plasmonic antennas," Opt. Express **19**, 5888–5894 (2011).
53. M. Galli, S. Portalupi, M. Belotti, L. Andreani, L. O'Faolain, and T. Krauss, "Light scattering and Fano resonances in high-*Q* photonic crystal nanocavities," Appl. Phys. Lett. **94**, 071101 (2009).
54. C. Zhou, S. Li, M. Fan, X. Wang, Y. Xu, W. Xu, S. Xiao, M. Hu, and J. Liu, "Optical radiation manipulation of Si-$Ge_2Sb_2Te_5$ hybrid metasurfaces," Opt. Express **28**, 9690–9701 (2020).
55. P. C. Wu, C. Y. Liao, V. Savinov, T. L. Chung, W. T. Chen, Y.-W. Huang, P. R. Wu, Y.-H. Chen, A.-Q. Liu, N. I. Zheludev, and D. P. Tsai, "Optical anapole metamaterial," ACS Nano **12**, 1920–1927 (2018).
56. S. Shen, Y. Wu, Y. Li, P. Xie, Q. Ding, X. Kuang, W. Wang, and W. Wang, "Tuning magnetic Mie-exciton interaction from the intermediate to strong coupling regime in a WSe_2 monolayer coupled with dielectric-metal nanoresonators," Phys. Rev. B **105**, 155403 (2022).
57. M. Yokoyama and S. Noda, "Finite-difference time-domain simulation of two-dimensional photonic crystal surface-emitting laser," Opt. Express **13**, 2869–2880 (2005).
58. V. A. Fedotov, N. Papasimakis, E. Plum, A. Bitzer, M. Walther, P. Kuo, D. Tsai, and N. Zheludev, "Spectral collapse in ensembles of metamolecules," Phys. Rev. Lett. **104**, 223901 (2010).
59. A. C. Overvig, S. Shrestha, and N. Yu, "Dimerized high contrast gratings," Nanophotonics **7**, 1157–1168 (2018).
60. D. C. Zografopoulos and V. Dmitriev, "Quasi-dark resonances in silicon metasurface for refractometric sensing and tunable notch filtering," J. Lightwave Technol. **39**, 6985–6993 (2021).
61. J. Algorri, F. Dell'Olio, P. Roldán-Varona, L. Rodrguez-Cobo, J. López-Higuera, J. Sánchez-Pena, V. Dmitriev, and D. Zografopoulos, "Analogue of electromagnetically induced transparency in square slotted silicon metasurfaces supporting bound states in the continuum," Opt. Express **30**, 4615–4630 (2022).